ARTICLE

Stannaborates: Tuning the Ion Conductivity of Dodecaborate Salts with Tin Substitution

Received 00th January 20xx,
Accepted 00th January 20xx

DOI: 10.1039/x0xx00000x

Thomas A. Hales [a], Kasper T. Møller [a,b], Terry D. Humphries [a], Anita M. D'Angelo [c], Craig E. Buckley [a], Mark Paskevicius [a*]

Metal substituted dodecaborate anions can be coupled with alkali metal cations to have great potential as solid-state ion conductors for battery applications. A tin atom can replace a B-H unit within an unsubstituted dodecaborate cage to produce a stable, polar divalent anion. The chemical and structural change in forming a stannaborate results in a modified crystal structure of respective group 1 metal salts, and as a result, improves the material's ion conductivity. $Li_2B_{11}H_{11}Sn$ shows high ion conductivity of ~ 8 mS cm^{-1} at 130 °C, similar to the state-of-the-art $LiCB_{11}H_{12}$ at these temperatures, however, obtaining high ion conductivity at room temperature is not possible with pristine alkali metal stannaborates.

Introduction

Energy storage devices are vital to solidify a green future as they allow renewable energy from intermittent sources to be stored and redistributed whenever needed throughout the day. Current electrical storage devices, or batteries, as they are more commonly known, traditionally contain two solid electrodes and a liquid electrolyte, e.g. containing a lithium salt in an organic solvent such as diethylene carbonate.[1] The role of the electrolyte is to allow ions to be transported from one electrode to the other. However, these liquid electrolytes have severe drawbacks for large scale energy storage, for example, they are flammable and volatile.[2] Also, liquid electrolytes do not allow for pure metal (e.g. lithium) electrodes to be used due to dangerous dendrite growth.[3] One way to combat these issues is to use a complete solid-state construction for the battery. This all-solid-state battery contains a solid-state electrolyte, which allows small metal cations to migrate through an anionic crystal lattice between the two solid electrodes.[4] Furthermore, an elemental metal cathode can be used which helps reduce the cost of the cell, improve the voltage window, and reduce the size and weight.[4]

There are many different types of compounds that have shown potential to be used as solid-state electrolytes. The most prevalent of these are inorganic ceramic solids such as sulphides (e.g. $Li_{10}GeP_2S_{12}$) and silicates (e.g. $Na_3Zr_2PSi_2O_{12}$).[5,6] They show promise due to the high lability of the respective lithium and sodium ions, resulting in high ion conductivity, especially at high temperature (> 100 °C), and importantly they are chemically stable with oxidative stabilities of 2.1 V for $Li_{10}GeP_2S_{12}$.[7] Inorganic solids, such as sulphides, are already being commercially used alongside a lithium metal anode and a lithium manganese oxide ($LiMn_2O_4$) cathode.[8] Other types of materials proposed as possible solid-state electrolytes are solvent-free salts or polymers. Polymeric electrolytes operate by the migration of metal ions through the polymer chain between the two electrodes, for example, in the work reviewed by Yue *et al.* where a variety of polymer mixtures are used to produce high ion conductivity levels.[9]

Borohydride salts have been shown to have high ion conductivity, in particular at high temperatures.[10] This is especially true for cluster borate salts, for example, *closo*-dodecaborate salts ($[B_{12}H_{12}]^{2-}$). These anions have been paired with different alkali metal cations such as lithium, sodium, and potassium and show excellent ionic conductivity performance at elevated temperatures, for example, $Li_2B_{12}H_{12}$ (8 x 10^{-2} S cm^{-1} at 280 °C), $Na_2B_{10}H_{10}$ (2 x 10^{-2} S cm^{-1} at 150 °C), and $KB_{11}H_{14}$ (1 × 10^{-4} S cm^{-1} at 150 °C).[11–14]

Substituted *closo*-dodecaborate cages have been known to improve the ion conductivity at lower temperatures in comparison to unsubstituted $B_{12}H_{12}^{2-}$ salts. $LiCB_{11}H_{12}$ and $NaCB_{11}H_{12}$ shows vastly improved performance at room and elevated temperature ($LiCB_{11}H_{12}$ ~ 0.1 S cm^{-1} at 120 °C), even for divalent cations.[11,15] The insertion of a carbon atom creates a dipole within the boron anion and changes the anion reorientational dynamics, which is believed to increase the ion conductivity.[16,17] Metal cations diffuse through the anionic lattice, possibly through a paddle-wheel mechanism, which reduces cation hopping energy and as a result improves the ion conductivity at a specific temperature.[18] Introducing a lead atom into the anion was also seen to show high ionic conductivity, however, not to the level of the 12-vertex carborane.[19] The lower ion conductivity displayed by these

[a] *Physics and Astronomy, Institute for Energy Transition, Curtin University, GPO Box U1987, Perth, WA 6845, Australia. E-mail: mark.paskevicius@gmail.com*
[b] *Department of Biological and Chemical Engineering, Aarhus University, Aabogade 40, Aarhus DK-8200, Denmark*
[c] *Australian Synchrotron (ANSTO), Clayton, VIC 3168, Australia*
† Footnotes relating to the title and/or authors should appear here.
Electronic Supplementary Information (ESI) available: [details of any supplementary information available should be included here]. See DOI: 10.1039/x0xx00000x

plumba-*closo*-dodecaborates could possibly be explained by them not demonstrating a polymorphic phase transition to a structure with high reorientational dynamics, which is present in the carboranes.

Stannaborates ($B_{11}H_{11}Sn^{2-}$ compounds) have been known for 30 years since their discovery by Chapman *et al.*[20] The prototypical stannaborate, $[Ph_3MeP]_2[B_{11}H_{11}Sn]$, was synthesised from a *nido*-borane precursor, $B_{11}H_{14}^-$, and has since been modified into a variety of different salts (e.g. NBu_4^+).[21] These compounds have been used in coordination chemistry, coordinating from the tin atom to a variety of metal centres such as Mo, Ru, and Ni.[21,22] When the salts are synthesised, they are usually coupled with a bulky organic cation and they have not yet been explored in regard to their ion conductivity. While organic cations are particularly useful in coordination chemistry, they cannot be used as solid-state electrolytes in battery applications. For this purpose, salts with a metal cation must be used. Solvated lithium and cesium stanna-*closo*-dodecaborates have previously been synthesised, and the synthesis of similar alkali metal salts with a $B_{11}H_{11}Pb^{2-}$ anion have also been achieved.[19,23] The aim of this research is to synthesise and characterise a variety of alkali metal stannaborate salts for their potential use as solid-state ion conductors.

Experimental

Density Functional Theory (DFT) was performed using the B3LYP hybrid functional with a LanL2MB basis set, in order to process the large Sn atom.[24–26] The calculations were performed using the software Gaussian G09W, optimising geometry and anion energy.[27] Electrostatic Potential (ESP) surfaces were mapped at an isovalue of 0.008 electrons/bohr^3. Atomic coordinates of the $B_{11}H_{11}Sn^{2-}$ anion are shown in Table S1.

Nuclear Magnetic Resonance (NMR) spectroscopy was performed on a Bruker AVANCE III 400 MHz spectrometer (128.4 MHz for ^{11}B) with proton decoupled spectra referenced to $BF_3{\cdot}OEt_2$ and Me_4Si respectively using a CD_3CN solvent.

Differential scanning calorimetry (DSC) was performed using a Netzsch STA 449 F3 Jupiter. The samples (~ 4 mg) were placed in a sealed aluminium crucible with a pinhole pierced into the lid and heated from 40 - 400 °C (10 °C min^{-1}) in an argon flow of 40 mL min^{-1}. The temperature and sensitivity of the DSC was calibrated using In, Zn, Sn, Bi, and CsCl reference materials, resulting in a temperature accuracy of ± 0.2 °C.

Electrochemical Impedance Spectroscopy (EIS) was measured using a ZIVE SP1 instrument. The compounds were pressed into pellets, with a diameter of 6 mm and thickness of ~ 1 mm, by applying a pressure of 1000 kg in an inert argon atmosphere. A pellet was placed between 2 gold wafers (0.1 mm thickness) and loaded into sealed Teflon sample cells with stainless steel electrodes under argon. The data were collected using AC voltage from 1 MHz to 10 Hz. To elucidate the ion conductivity (σ) from the data, the *x*-intercept (Z_{real}) of the Nyquist plot was determined using a known literature method, see Figure S1. [28]

Linear Sweep Voltammetry (LSV) was performed to determine the oxidative stability limit of the $Li_2B_{11}H_{11}Sn$ salt against Li metal. The method used was based on a method proposed by Han *et al.* and Asakura *et al.* [7,29] $Li_2B_{11}H_{11}Sn$ was mixed with graphite (Sigma Aldrich, powder < 20 µg), previously heated to 550 °C under vacuum for 12 h, in a weight ratio of 75:25 by grinding 5 times with a mortar and pestle. 3 mg of the mixture was layered on top of 40 mg of pristine $Li_2B_{11}H_{11}Sn$ and pressed together at 2000 kg in an inert argon atmosphere to form a two layered pellet. This pellet was sandwiched to form an Al/Pt/Sample+C/Sample/Li configuration, which was sealed within an air-tight Teflon cell. LSV was conducted at 60 °C with a scan rate of 50 µV s^{-1} from the open circuit voltage (2.3 V) to 8 V. A second LSV cycle was also conducted from 1 - 5.2 V at the same scan rate and temperature to verify subsequent reactions. The oxidative stability of the material was determined from the intersection point of the background and the oxidative current.[29]

In-situ and ex situ Synchrotron Radiation – X-Ray Diffraction (SR-XRD) data were collected on the powder diffraction (PD) beamline at the Australian Synchrotron using a Mythen-II strip detector with at a scan rate of 30 secs scan^{-1} using a wavelength of 0.59096(1) Å. All samples were packed in borosilicate capillaries (inner diameter – 0.7 mm) and flame sealed under an argon atmosphere. The samples were heated to 327 °C using a hot air blower at 5 °C min^{-1}. Sample temperatures were calibrated against the known lattice parameter of silver as a function of temperature.[30] Crystallographic indexing was performed in Topas v.5 (Bruker, Germany).

Raman Spectroscopy was performed using a WITec Alpha 300 SAR confocal Raman microscope with a 532 nm green light excitation wavelength and 600 grating/mm. Samples were prepared in 1 mm wide borosilicate capillaries in an Ar filled glovebox then flame sealed to prevent exposure to air and moisture. Spectra were collected with 100 accumulations with an integration time of 400 ms. Data processing including background subtraction was performed using Project 4 (WITec) software.

Lithium hydroxide (98%, −4 +1 4 mesh, anhydrous, Alfa Aesar), anhydrous sodium hydroxide (reagent grade, ≥ 98%, pellets, Sigma-Aldrich), potassium hydroxide (technical, ≥ 85% powder, Sigma-Aldrich), tin (II) chloride (98%, Sigma-Aldrich), and hydrochloric acid (37%, Fisher) were all used as purchased or diluted to desired concentrations using Milli-Q water. $(CH_3)_3NHB_{11}H_{14}$ was prepared using the method of Dunks *et al.* from sodium borohydride (98% (0.5% $MgCO_3$), Sigma-Aldrich) and 1-bromopentane (98%, Sigma-Aldrich) in diglyme (99.5%, anhydrous, Sigma-Aldrich).[31] The synthesis involves dissolving sodium borohydride in diglyme followed by the drop-wise addition of 1-bromopentane at 105 °C for 4h, and subsequent room temperature precipitation from water using

trimethylammonium chloride (Sigma-Aldrich). All samples were prepared and stored under an inert argon atmosphere.

Synthesis of $Li_2B_{11}H_{11}Sn$

The synthesis method was an adaption of that reported by Gädt and Wesemann.[23] $(CH_3)_3NHB_{11}H_{14}$ (2.600 g, 13.46 mmol) was dissolved in anhydrous tetrahydrofuran (THF) (40 mL) and cooled to 0 °C before *n*-butyllithium (30 mL) was added dropwise and the solution was stirred for 30 minutes under an inert argon atmosphere. Tin (II) chloride (3.70 g, 19.51 mmol) dissolved in THF (30 mL) was added dropwise to the pale yellow solution at room temperature. The solution turned deep red instantaneously and was stirred for a further 4 hours at room temperature. THF was removed using rotary evaporation and the dry product was dissolved in aqueous lithium hydroxide (1M, 50 mL) to extract the product from the resulting mixture. The solution was filtered *in vacuo* and the filtrate neutralised to pH 7 using HCl (1 M). The solvent was removed *in vacuo* and acetonitrile (15 mL) was added to the resulting solid, which helps to remove the LiCl by-product. The suspension was filtered and the filtrate was dried *in vacuo* at 150 °C leaving a pale yellow, highly hygroscopic solid, which was stored under argon, $Li_2B_{11}H_{11}Sn$ (2.083 g, 7.93 mmol, 59% yield). $^{11}B\{^1H\}$ NMR (128 MHz, CD_3CN) –5.3 (s, 1B), -11.1 (s, 5B), -12.4 (s, 5B). $^1H\{^{11}B\}$ NMR (400 MHz, CD_3CN) 2.98 (s, 1H), 1.60 (s, 5H), 0.82 (s, 5B).

Synthesis of $M_2B_{11}H_{11}Sn$ (M = Na, K)

$Li_2B_{11}H_{11}Sn$ (0.215 g, 0.819 mmol) was dissolved in water (5 mL) and passed through a column containing Amberlite® IR 120 hydrogen form ion exchange resin. The resulting acidic solution was treated with the relevant metal hydroxide (NaOH or KOH) until pH 7. The water was removed *in vacuo* at 150 °C leaving the desired product, $Na_2B_{11}H_{11}Sn$ (0.201 g, 84% yield) or $K_2B_{11}H_{11}Sn$ (68% yield).

Results and Discussion

The use of a stannaborate salt as a solid-state electrolyte provides an alternative to a carborane salt, which may hold similar anionic polarity due to the similarity between charge distribution in the anion. It is postulated that a polarised anionic charge distribution may allow for favourable reorientational anion dynamics in the solid-state, thus providing similar levels of high ion conductivity as the carborane. The replacement of Sn for C-H may also change the temperature at which rapid reorientational dynamics are observed via a lower temperature polymorphic phase transition. To understand the charge distribution in the stannaborate anion a theoretical calculation can be undertaken computationally and compared to similar anions. Figure 1 shows the calculated electrostatic potential surfaces of various borane anions. The introduction of a heteroatom into the 12-vertex borane anion creates a permanent electrostatic dipole with electron density moving away from the heteroatom in the case of carborane. The lithium and sodium salts of the 12-vertex carborane ($CB_{11}H_{12}^-$) show vastly improved ion conductivity compared with the respective unsubstituted $B_{12}H_{12}^{2-}$ salts.[11] The overall charge is higher for the divalent $B_{11}H_{11}Sn^{2-}$ anion compared to the monovalent $CB_{11}H_{12}^-$. A major difference between the carborane and stannaborate anions is the fact that the carbon is protonated, whilst the tin atom is not. As such, it is clear from Figure 1 that whilst the C-H unit in the carborane forms a less-negative node, the Sn atom forms a more-negative node, in contrast to the B-H units in the respective anions. Despite the different charge distribution in the stannaborate compared to carborane anion, a noticeable polarity to the charge is present. The length of the $B_{11}H_{11}Sn^{2-}$, measured from Sn-H1 is 5.446 Å, which is similar to the total length of $CB_{11}H_{12}^-$ (5.524 Å when measured CH-H1) despite the Sn not being protonated. This is due to the disproportionate size of the tin atom being similar to a C-H unit. The unsubstituted $B_{12}H_{12}^{2-}$ is slightly larger (5.833 Å) than the carborane due to the fact the carbon atom sits further down into the cage. The resulting crystal structure of a solid-state salt can be influenced by the charge distribution of the ions. In the case of respective borates, the anionic polarity (or lack of) will affect the respective cation locations with respect to the anion due to electrostatic forces and steric constraints.[32] The resulting crystal structure will change the cationic conductive mechanisms and pathways through the anionic lattice. Therefore, the calculated charge distribution of the stannaborate anion provides indications that it may form favourable alkali metal salts.

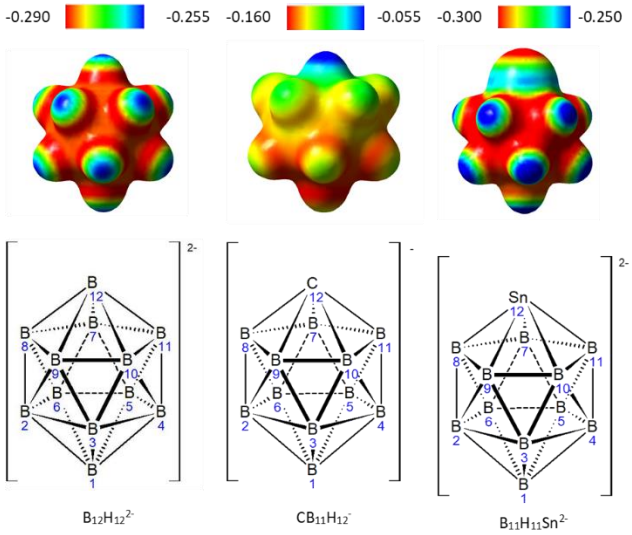

Figure 1: Electrostatic potential surfaces and structures (without hydrogen shown) of *closo*-borate anions optimised and generated using a B3LYP/LanM2MB basis set (Total Self-Consistent Field (SCF) Density (isovalue = 0.008)). NOTE: Sn atom is not protonated.

The synthesis of the $B_{11}H_{11}Sn^{2-}$ anion follows the same synthetic pathways as its sister compounds $CB_{11}H_{12}^-$ and $B_{11}H_{11}Pb^{2-}$.[20,33] An open 11-vertex borane anion ($B_{11}H_{14}^-$) is deprotonated by a base and a non-boron heteroatom is inserted into the anion to form a *closo*-undecaborate anion containing the atom of choice.

The method used follows that described by Chapman *et al.* using a $Me_3NHB_{11}H_{14}$ precursor treated with a strong base, in this case *n*BuLi, and reacted with $SnCl_2$ in a THF solvent under an inert atmosphere.[20] Due to the increased stability of $SnCl_2$ compared with its carbon analogue, CCl_2, which can only be made *in-situ*, it can instead be added directly as a reagent. This synthetic route has also previously been used to synthesise stannaborate salts with bulky organic cations or solvated lithium or cesium.[23] The synthesis of alkali metal stannaborate salts is achieved by modifications to the original synthetic procedure reported by Chapman *et al*.[20] It should also be noted that anhydrous $SnCl_2$ must be used as insertion reactions since hydrated $SnCl_2{\cdot}2H_2O$ was attempted but did not result in the insertion of a Sn atom into the borane cage. Furthermore, aqueous bases such as hydroxides cannot be used for the same reason in the initial anion synthesis. In contrast, the synthesis of $B_{11}H_{11}Pb^{2-}$ salts utilise aqueous bases due to two main factors: the maintained activity of the aqueous $PbCl_2$ reagent, and the avoidance of highly toxic butyl lead when *n*BuLi is reacted with Pb compounds.

The $B_{11}H_{11}Sn^{2-}$ anion was successfully synthesised and confirmed by ^{11}B NMR spectroscopy (see Figure 2a). It shows three characteristic resonances at -5.3 (B1), -11.1 (B2-B6) and -12.4 (B7-B11) ppm with an intensity ratio 1:5:5, which correlates to the three different boron environments within the anion structure (B1, B2-B6, B7-B11 in Figure 1). Interestingly, there are shoulders on the resonance seen at -11.1 ppm. These arise from the coupling of the boron atoms to the tin atom, which has a low abundance (7.7 %) NMR active (I = ½) isotope that causes peak splitting of the singlet.[34] The interaction between the Sn and adjacent B's creates a triplet arising from the spin active (I = ½) and inactive (I = 0) tin nuclei, respectively, which was also seen in the NMR spectrum of $B_{11}H_{11}Pb^{2-}$.[19] The ^1H {^{11}B} NMR spectra shows 3 major resonances (2.98, 1.60 and 0.82 ppm) alongside two solvent signals at 2.8 and 1.9 ppm corresponding to acetonitrile and water.[35] There is a small $B_{11}H_{11}^{2-}$ impurity (~ 2.5% based on ^{11}B integration) arising from premature closing of the boron-cage after deprotonation, but before Sn insertion. This is not believed to have a major impact on the bulk ion conductivity or thermal characteristics. The sodium and potassium salts show the same NMR spectra as they weren't synthesised from the lithium analogue using cation exchange.

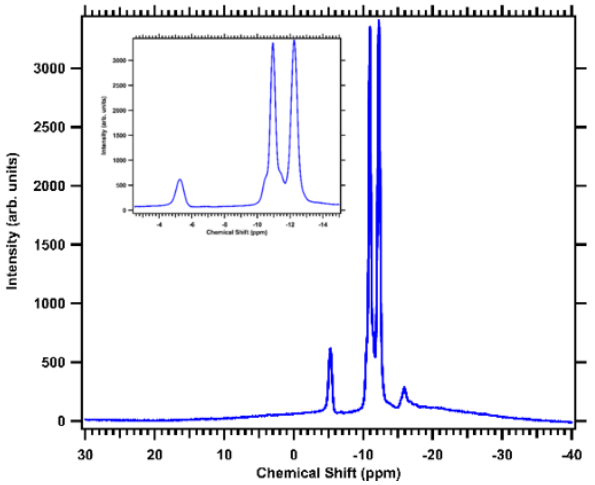

Figure 2a: ^{11}B {^1H} NMR spectrum of $Li_2B_{11}H_{11}Sn$ in CD_3CN: –5.3 (s, 1B, B1), -11.1 (s, 5B, B7-B11), -12.4 (s, 5B, B2-B6).

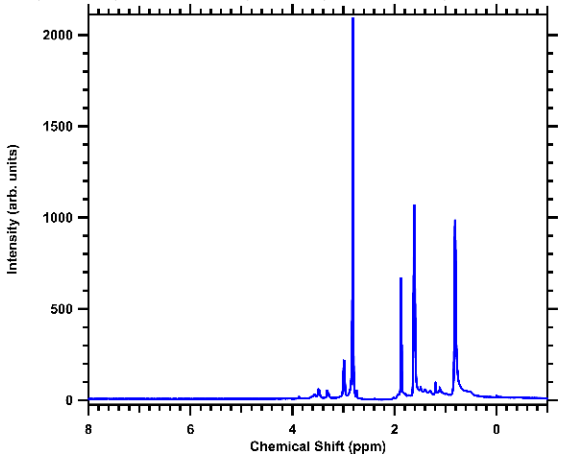

Figure 2b: ^1H {^{11}B} NMR spectrum of $Li_2B_{11}H_{11}Sn$ in CD_3CN: 2.98 (s, 1H), 1.60 (s, 5H), 0.82 (s, 5H)

The lithium stannaborate salt was analysed using Raman spectroscopy (Figure 3) under an inert argon atmosphere in a sealed capillary. The spectrum contains a strong signal at ~ 2450 cm^{-1} that corresponds to a B-H stretch within the $B_{11}H_{11}Sn^{2-}$ cage. There are 3 other major signals in the spectrum at 750, 570, and 280 cm^{-1}. These correspond to vibrational modes connected to the stretching modes of the stannaborate cage. The signals at 750 and 570 cm^{-1} correspond to similar modes seen the in mono-carborane anion ($CB_{11}H_{12}^-$) due to the stretching and deformation of a boron cage. The very strong peak at 280 cm^{-1} is not seen in the case of the carborane, owing to the signal corresponding to the stretch of the B-Sn bond, which is consistent with the computational pattern in Figure 3. The low frequency of the stretch is due to the high mass of the Sn atom in comparison to a boron or carbon atom. The Raman spectrum for the lithium stannaborate salt also correlates well with one previously reported for cesium stannaborate.[23] Thus, the Raman and NMR data show that the $B_{11}H_{11}Sn^{2-}$ anion has been successfully synthesised.

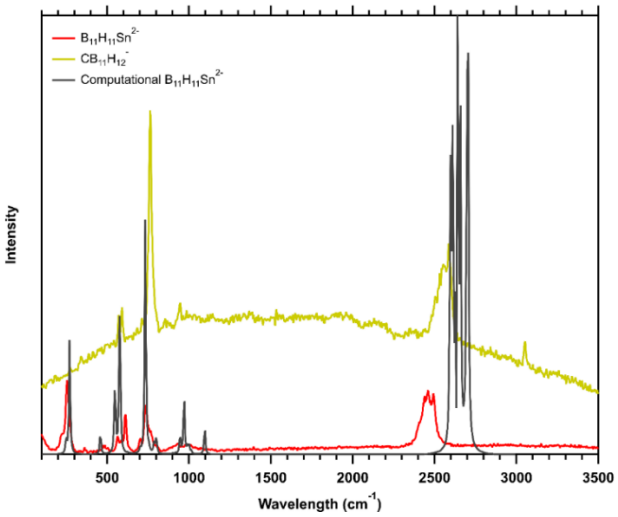

Figure 3: Experimental Raman spectroscopy of $Li_2B_{11}H_{11}Sn$ and $Zn(CB_{11}H_{12})_2$ performed in an inert argon atmosphere compared with a computational spectrum of $B_{11}H_{11}Sn^{2-}$.

Figure 4 shows the DSC analysis of the lithium, sodium, and potassium stannaborate salts. All samples show a distinct endothermic peak at different temperatures, which could be synonymous with a variety of different structural and chemical processes. $Li_2B_{11}H_{11}Sn$ shows this endothermic event at 340 °C with $Na_2B_{11}H_{11}Sn$ at 180 °C and $K_2B_{11}H_{11}Sn$ at 250 °C, respectively.

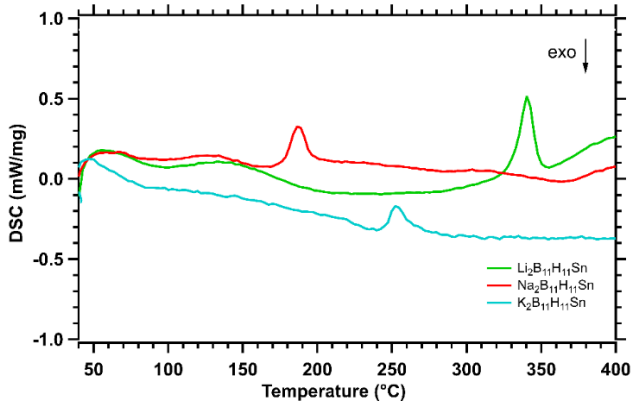

Figure 4: DSC analysis of alkali metal $B_{11}H_{11}Sn^{2-}$ salts in an argon atmosphere at 5 °C min^{-1}.

In-situ SR-XRD was performed on the stannaborates in an attempt to understand the endothermic events observed during DSC analysis with the data illustrated in Figure 5 and Figures S2-S6. The data for the $Li_2B_{11}H_{11}Sn$ sample (Figure 5a) illustrates that pattern at 30 °C contains at least two crystallographic phases. One of these phases is LiCl, an impurity, which persists throughout heating and cooling of the material. One phase decomposes at ~ 65 °C and is likely attributed to a dehydration step, where hydration of the sample occurred during exposure to air when sealing the capillary due to the fact that no characteristic water signals are seen in the Raman spectrum. It should be noted that none of the observed phases match the known $[Li(thf)_3]_2[SnB_{11}H_{11}]$ crystal structure, indicating again that the lithium stannaborate is likely hydrated, rather than solvated by tetrahydrofuran, as shown by NMR.[23] Another major phase exists that undergoes an increase of crystallographic symmetry at 130 °C, possibly due to the full or partial dehydration of the material. Indexing of the diffraction pattern determined a tetragonal space group ($P4_2/ncm$) with lattice parameters of $a = b = 9.8923(4)$ Å and $c = 10.4149(3)$ Å. This phase is present until ~ 330 °C when decomposition occurs forming an amorphous phase which is apparent through a halo around $2\Theta = 6°$, which is also seen after the decomposition of similar compounds such as $Li_2B_{11}H_{11}Pb$.[19] These observations are corroborated in the DSC data (Figure 4), where endothermic events occur at peak temperatures of 60, 130, and 340 °C, respectively. After decomposition, the crystallisation of Sn metal is seen.

$Na_2B_{11}H_{11}Sn$ and $K_2B_{11}H_{11}Sn$ also show their respective metal chloride (NaCl and KCl) impurities, which persist throughout the heating process (Figure 5b and 5c). The room temperature phase of $K_2B_{11}H_{11}Sn$ has been indexed to exist in an orthorhombic space group with $a = 11.7216(3)$, $b = 8.1006(1)$, and $c = 12.0948(3)$ Å, although the crystal structure could not explicitly be solved. The room temperature data for $Na_2B_{11}H_{11}Sn$ could not be indexed due to the poor crystallinity of the sample. Upon heating, these compounds behave differently to the lithium analogue. They have a reversible polymorphic phase change at 200 °C and 250 °C, respectively, which explains the endothermic peaks seen in DSC (Figure 4). These high temperature phase changes for $Na_2B_{11}H_{11}Sn$ and $K_2B_{11}H_{11}Sn$ occur at higher temperatures than seen in the lithium and sodium 12-vertex carborane.[36] High temperature polymorphic phase transitions can be favourable in enhancing the ion conductivity of a material, as seen in this class of boron-based compounds.[37] However, this is an improvement on $B_{11}H_{11}Pb^{2-}$ salts due to the fact there are no polymorphic phase transitions before decomposition. The high temperature phase changes are also coupled by the appearance of a halo at $2\Theta = 4.2°$ and indicates the formation of an amorphous phase, which is different to the decomposition halo seen in $Li_2B_{11}H_{11}Sn$, which is seen at $2\Theta = 6.2°$. This is also seen as a decomposition product, such as $Li_2B_{12}H_{12}$.[38] Upon cooling, both the $Na_2B_{11}H_{11}Sn$ and $K_2B_{11}H_{11}Sn$ materials return to their low temperature phases as the decomposition temperature of these materials were not attained.

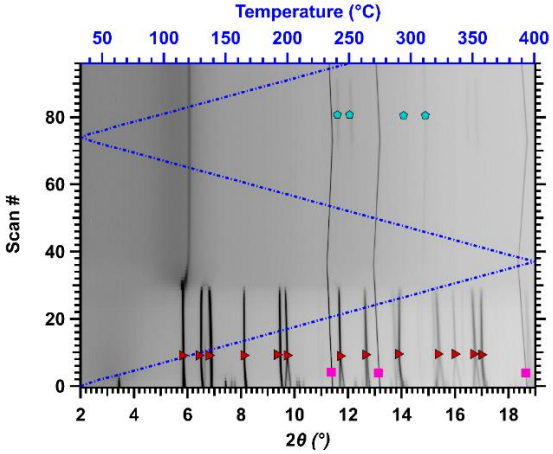

Figure 5a: *In-situ* XRD spectrum of $Li_2B_{11}H_{11}Sn$ heated at 5 °C min^{-1} and λ = 0.59096(1) Å. Pink square – LiCl, Blue pentagon – Sn metal. Blue dashed line signifies temperature for a specific scan.

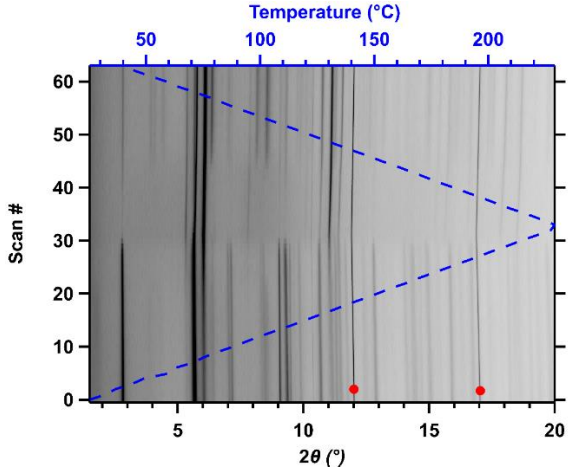

Figure 5b: *In-situ* XRD spectrum of $Na_2B_{11}H_{11}Sn$ heated at 5 °C min^{-1} and λ = 0.59096(1) Å. Red circle – NaCl. Blue dashed line signifies temperature for a specific scan.

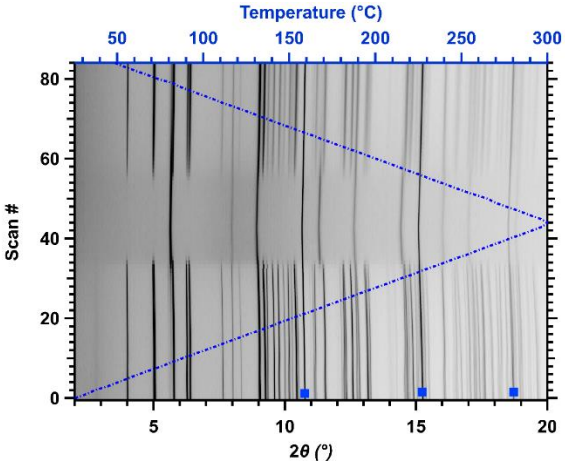

Figure 5c: *In-situ* XRD spectrum of $K_2B_{11}H_{11}Sn$ heated at 5 °C min^{-1} and λ = 0.59096(1) Å. Blue square – KCl. Blue dashed line signifies temperature for a specific scan.

The stannaborate salts were analysed by EIS to assess their ion conductivity as a function of temperature and determine their suitability as solid-state ion conductors (Figure 6). All of the materials show low, but measurable ion conductivity at room temperature but improve greatly on heating. $Li_2B_{11}H_{11}Sn$ shows promise as it reaches superionic conductivity (> 1 x 10^{-3} S cm^{-1}) above 110 °C. The ion conductivity reaches a maximum of 8 x 10^{-3} S cm^{-1} at 130 °C, however, the ion conductivity decreases at higher temperature, which corresponds with an event seen in the *in-situ* XRD, attributed to desolvation (Figure 5a). Desolvation is known to have an effect on the ion conductivity of solid-state ion conductors.[14] Thus, the ion conductivity for $Li_2B_{11}H_{11}Sn$ is lower than $Li_2B_{11}H_{11}Pb$ (2 x 10^{-2} S cm^{-1} at 120 °C)[19] and $LiCB_{11}H_{12}$ (2 x 10^{-1} at 150 °C)[11], but does show a higher ion conductivity than the unsubstituted $Li_2B_{12}H_{12}$ above 110 °C. $Na_2B_{11}H_{11}Sn$ shows promise reaching 1 x 10^{-3} S cm^{-1} at 170 °C, which is a large improvement in comparison to its contemporaries $Na_2B_{11}H_{11}Pb$ (1 x 10^{-5} S cm^{-1} at 170 °C)[19] and the unsubstituted $Na_2B_{12}H_{12}$ (1 x 10^{-4} S cm^{-1} at 170 °C)[39]. $K_2B_{11}H_{11}Sn$ shows low ion conductivity of 1 x 10^{-6} S cm^{-1} at 100 °C, much lower than $KB_{11}H_{14}$ (1 × 10^{-4} S cm^{-1} at 150 °C) and slightly better than to KB_3H_8 (2 x 10^{-7} S cm^{-1} at 150 °C).[12,40] The ion conductivity results for the stannaborates in comparison to other borate salts demonstrate that superionic conductivities are obtainable, but it is still difficult to predict which borate salts will present superionic conductivity at (or near) room temperature. High ion conductivity is most often linked to rapid reorientational dynamics, but also structural considerations, including anion size, anion electrostatic polarity, cation size, and structure-type.[28,37,41] Therefore, the search for a room temperature superionically conducting salt still requires further experimental and theoretical studies to determine the optimum chemical compositions and structures.

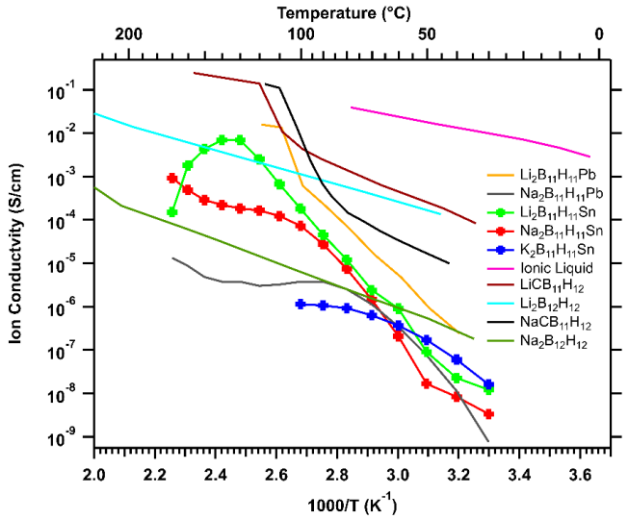

Figure 6: Ion conductivity of stannaborates and comparable salts from literature.[11,19,37,42]

Linear sweep voltammetry (LSV) was performed on $Li_2B_{11}H_{11}Sn$ to assess the oxidative stability of the material, which shows the electrochemical limit where the compound is irreversibly oxidised. Thus, this shows the working range of these materials

as a possible solid-state electrolyte. $Li_2B_{11}H_{11}Sn$ shows immediate, irreversible oxidation from the open circuit voltage of 2.3 V vs Li^+/Li (Figure 7). This value is compared to other borate salts such as $LiBH_4$ (2.2 V), $Li_2B_{11}H_{11}Pb$ (2.3 V), and $LiB_{11}H_{14}{\cdot}xH_2O$ (2.9 V).[12,19,29] The oxidation event in Figure 7 is only observable in the first LSV scan, showing that it only occurs on the first voltage cycle as the electrolyte is already oxidised.

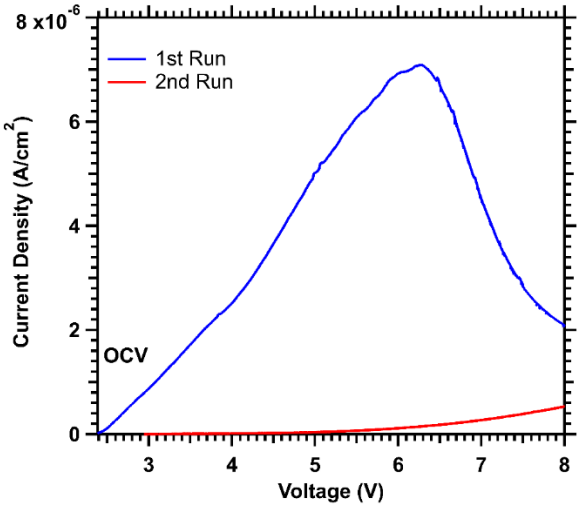

Figure 7: Linear Sweep Voltammetry chart of $Li_2B_{11}H_{11}Sn$ at 60 °C with a scan rate of 50 μV s^{-1} from the open circuit voltage (2.3 V) to 8 V.

Conclusions

A series of group 1 metal stanna-*closo*-dodecaborate salts were successfully synthesised from trimethylammonium *nido*-undecaborate. This was confirmed using ^{11}B and ^{1}H NMR along with computational and experimental Raman spectroscopy. Additional characterisation of these compounds included SR-XRD and DSC, which showed polymorphic phase changes in $Na_2B_{11}H_{11}Sn$ and $K_2B_{11}H_{11}Sn$ at 200 and 250 °C, respectively, and a decomposition event at 340 °C for $Li_2B_{11}H_{11}Sn$. The compounds showed crystalline structures and a high temperature polymorph of $K_2B_{11}H_{11}Sn$ could be indexed having an orthorhombic space group however, the full crystal structure of these compounds could not be determined. $Li_2B_{11}H_{11}Sn$ showed excellent ion conductivity above 1 mS cm^{-1} between 110 and 130 °C, however, the conductivity reduces at higher temperatures and correlates with a polymorphic phase change (increase in symmetry) seen in the *in-situ* SR-XRD diffraction pattern. $Na_2B_{11}H_{11}Sn$ also shows superionic conductivity at 170 °C and has higher conductivity than the lead analogue, however, once more, lower than $NaCB_{11}H_{12}$. It is thought that the ion conductivity of these compounds is lower than the carborane due to divalent nature of these salts. One way to improve the conductivity could be to introduce elements into the cage resulting in a monovalent anion.

Author Contributions

Thomas Hales – Conceptualisation, formal analysis, investigation (synthesis and characterisation), methodology, writing – original draft, writing – review and editing.

Kasper Møller – Investigation (initial synthetic study), writing – review and editing.

Terry Humphries – Investigation (SR-XRD analysis), supervision, writing – review and editing.

Anita D'Angelo – Investigation (SR-XRD acquisition), writing – review and editing.

Craig Buckley – Funding acquisition, supervision, writing – review and editing.

Mark Paskevicius – Conceptualisation, funding acquisition, project administration, supervision, writing – review and editing.

Conflicts of interest

There are no conflicts to declare.

Acknowledgements

MP, CEB, and TDH acknowledge the support of the Australian Research Council (ARC) for Discovery Project DP230100429. MP acknowledges the ARC for Future Fellowship FT160100303. TH acknowledges the support from Curtin International Postgraduate Research Scholarship (CIPRS) and Research Stipend Scholarship. KTM acknowledges the financial support from the Independent Research Fund Denmark (International Post doc Grant 8028-00009B) and the Carlsberg Foundation (Reintegration Fellowship CF19-0465). This research was undertaken on the Powder Diffraction beamline at the Australian Synchrotron, part of ANSTO.

Notes and references

1 Y. Nishi, *J. Power Sources*, 2001, **100**, 101–106.
2 P. G. Balakrishnan, R. Ramesh and T. Prem Kumar, *J. Power Sources*, 2006, **155**, 401–414.
3 O. Crowther and A. C. West, *J. Electrochem. Soc.*, 2008, **155**, A806.
4 J. G. Kim, B. Son, S. Mukherjee, N. Schuppert, A. Bates, O. Kwon, M. J. Choi, H. Y. Chung and S. Park, *J. Power Sources*, 2015, **282**, 299–322.
5 A. Hooper, *J. Electroanal. Chem.*, 1980, **109**, 161–166.
6 L. Schweiger, K. Hogrefe, B. Gadermaier, J. L. M. Rupp and H. M. R. Wilkening, *J. Am. Chem. Soc.*, 2022, **144**, 9597–9609.
7 F. Han, Y. Zhu, X. He, Y. Mo and C. Wang, *Adv. Energy Mater.*, 2016, **6**, 1–9.
8 Q. Zhang, D. Cao, Y. Ma, A. Natan, P. Aurora and H. Zhu, *Adv. Mater.*, 2019, **31**, 1–42.
9 L. Yue, J. Ma, J. Zhang, J. Zhao, S. Dong, Z. Liu, G. Cui and L. Chen, *Energy Storage Mater.*, 2016, **5**, 139–164.

10 F. Cuevas, M. B. Amdisen, M. Baricco, C. E. Buckley, Y. W. Cho, P. De Jongh, L. M. De Kort, J. B. Grinderslev, V. Gulino, B. C. Hauback, M. Heere, T. Humphries, T. R. Jensen, S. Kim, K. Kisu, Y. S. Lee, H. W. Li, R. Mohtadi, K. T. Møller, P. Ngene, D. Noréus, S. I. Orimo, M. Paskevicius, M. Polanski, S. Sartori, L. N. Skov, M. H. Sørby, B. C. Wood, V. A. Yartys, M. Zhu and M. Latroche, *Prog. Energy*, 2022, **4**, 032001.

11 W. S. Tang, A. Unemoto, W. Zhou, V. Stavila, M. Matsuo, H. Wu, S. I. Orimo and T. J. Udovic, *Energy Environ. Sci.*, 2015, **8**, 3637–3645.

12 D. H. P. Souza, K. T. Møller, S. A. Moggach, T. D. Humphries, A. M. D'Angelo, C. E. Buckley and M. Paskevicius, *J. Mater. Chem. A*, 2021, **9**, 15027–15037.

13 D. H. P. Souza, A. M. D'Angelo, C. E. Buckley, M. Paskevicius and T. D. Humphries, *Dalt. Trans.*, 2022, **51**, 13848–13857.

14 D. H. P. Souza, T. D. Humphries, Y. Liu, A. Gradišek, A. M. D'Angelo, C. E. Buckley and M. Paskevicius, *Sustain. Energy Fuels*, 2022, **6**, 4614–4625.

15 A. Berger, A. Ibrahim, C. E. Buckley and M. Paskevicius, *Phys. Chem. Chem. Phys.*, 2023, **25**, 5758–5775.

16 M. Dimitrievska, H. Wu, V. Stavila, O. A. Babanova, R. V. Skoryunov, A. V. Soloninin, W. Zhou, B. A. Trump, M. S. Andersson, A. V. Skripov and T. J. Udovic, *J. Phys. Chem. C*, 2020, **124**, 17992–18002.

17 K. Sau, T. Ikeshoji, S. Kim, S. Takagi and S. Orimo, *Chem. Mater.*, 2021, **33**, 2357–2369.

18 M. Paskevicius, B. R. S. Hansen, M. Jørgensen, B. Richter and T. R. Jensen, *Nat. Commun.*, 2017, **8**, 10–15.

19 T. A. Hales, K. T. Møller, T. D. Humphries, A. M. D'Angelo, C. E. Buckley and M. Paskevicius, *J. Phys. Chem. C*, 2023, **127**, 949–957.

20 R. W. Chapman, J. G. Kester, K. Folting, W. E. Streib and L. J. Todd, *Inorg. Chem.*, 1992, **31**, 979–983.

21 L. Wesemann, T. Marx, U. Englert and M. Ruck, *Eur. J. Inorg. Chem.*, 1999, 1563–1566.

22 T. Gädt, B. Grau, K. Eichele, I. Pantenburg and L. Wesemann, *Eur. J.*, 2006, 1036–1045.

23 T. Gädt and L. Wesemann, *Zeitschrift fur Anorg. und Allg. Chemie*, 2007, **633**, 693–699.

24 W. R. Wadt and P. J. Hay, *J. Chem. Phys.*, 1985, **82**, 284–298.

25 P. J. Hay and W. R. Wadt, *J. Chem. Phys.*, 1985, **82**, 270–283.

26 P. J. Hay and W. R. Wadt, *J. Chem. Phys.*, 1985, **82**, 299–310.

27 M. J. Frisch, G. W. Trucks, H. B. Schlegel, G. E. Scuseria, M. A. Robb, J. R. Cheeseman, G. Scalmani, V. Barone, G. A. Petersson, H. Nakatsuji, X. Li, M. Caricato, A. V. Marenich, J. Bloino, B. G. Janesko, R. Gomperts, B. Mennucci, H. P. Hratchian, J. V. Ortiz, A. F. Izmaylov, J. L. Sonnenberg, Williams, F. Ding, F. Lipparini, F. Egidi, J. Goings, B. Peng, A. Petrone, T. Henderson, D. Ranasinghe, V. G. Zakrzewski, J. Gao, N. Rega, G. Zheng, W. Liang, M. Hada, M. Ehara, K. Toyota, R. Fukuda, J. Hasegawa, M. Ishida, T. Nakajima, Y. Honda, O. Kitao, H. Nakai, T. Vreven, K. Throssell, J. A. Montgomery Jr., J. E. Peralta, F. Ogliaro, M. J. Bearpark, J. J. Heyd, E. N. Brothers, K. N. Kudin, V. N. Staroverov, T. A. Keith, R. Kobayashi, J. Normand, K. Raghavachari, A. P. Rendell, J. C. Burant, S. S. Iyengar, J. Tomasi, M. Cossi, J. M. Millam, M. Klene, C. Adamo, R. Cammi, J. W. Ochterski, R. L. Martin, K. Morokuma, O. Farkas, J. B. Foresman and D. J. Fox, *Gaussian 09, Revis. A. 02*, 2009.

28 B. R. S. Hansen, M. Paskevicius, M. Jørgensen and T. R. Jensen, *Chem. Mater.*, 2017, **29**, 3423–3430.

29 R. Asakura, L. Duchêne, R. S. Kühnel, A. Remhof, H. Hagemann and C. Battaglia, *ACS Appl. Energy Mater.*, 2019, **2**, 6924–6930.

30 I. K. Suh, H. Ohta and Y. Waseda, *J. Mater. Sci.*, 1988, **23**, 757–760.

31 G. B. Dunks, K. Barker, E. Hedaya, C. Hefner, K. Palmer-Ordonez and P. Remec, *Inorg. Chem.*, 1981, **20**, 1692–1697.

32 Z. Zhang and L. F. Nazar, *Nat. Rev. Mater.*, 2022, **7**, 389–405.

33 A. Berger, C. E. Buckley and M. Paskevicius, *Inorg. Chem.*, 2021, **60**, 14744–14751.

34 E. Scientific, P. Company, C. Devillers, T. Lecomte and R. Hagemann, 1983, **50**, 205–217.

35 G. R. Fulmer, A. J. M. Miller, N. H. Sherden, H. E. Gottlieb, A. Nudelman, B. M. Stoltz, J. E. Bercaw, K. I. Goldberg, R. Gan and H. Apiezon, *Organometallics*, 2010, **29**, 2176–2179.

36 T. J. Udovic, M. Matsuo, W. S. Tang, H. Wu, V. Stavila, A. V. Soloninin, R. V. Skoryunov, O. A. Babanova, A. V. Skripov, J. J. Rush, A. Unemoto, H. Takamura and S. I. Orimo, *Adv. Mater.*, 2014, **26**, 7622–7626.

37 B. R. S. Hansen, M. Paskevicius, H. W. Li, E. Akiba and T. R. Jensen, *Coord. Chem. Rev.*, 2016, **323**, 60–70.

38 M. P. Pitt, M. Paskevicius, D. H. Brown, D. A. Sheppard and C. E. Buckley, *J. Am. Chem. Soc.*, 2013, **135**, 6930–6941.

39 T. J. Udovic, M. Matsuo, A. Unemoto, N. Verdal, V. Stavila, A. V. Skripov, J. J. Rush, H. Takamura and S. I. Orimo, *Chem. Commun.*, 2014, **50**, 3750–3752.

40 J. B. Grinderslev, K. T. Møller, Y. Yan, X. M. Chen, Y. Li, H. W. Li, W. Zhou, J. Skibsted, X. Chen and T. R. Jensen, *Dalt. Trans.*, 2019, **48**, 8872–8881.

41 M. Jørgensen, P. T. Shea, A. W. Tomich, J. B. Varley, M. Bercx, S. Lovera, R. Černý, W. Zhou, T. J. Udovic, V. Lavallo, T. R. Jensen, B. C. Wood and V. Stavila, *Chem. Mater.*, 2020, **32**, 1475–1487.

42 Y. Sadikin, M. Brighi, P. Schouwink and R. Černý, *Adv. Energy Mater.*, 2015, **5**, 1501016.